Segmentation-Free Velocity Field Super-Resolution on 4D Flow MRI

Sébastien Levilly, Saïd Moussaoui, Jean-Michel Serfaty

Segmentation-Free Velocity Field Super-Resolution on 4D Flow MRI

Sébastien Levilly, Saïd Moussaoui, *Member, IEEE*, and Jean-Michel Serfaty

***Abstract*—Blood flow observation is of high interest in cardiovascular disease diagnosis and assessment. For this purpose, 2D Phase-Contrast MRI is widely used in the clinical routine. 4D flow MRI sequences, which dynamically image the anatomic shape and velocity vectors within a region of interest, are promising but rarely used due to their low resolution and signal-to-noise ratio (SNR). Computational fluid dynamics (CFD) simulation is considered as a reference solution for resolution enhancement. However, its precision relies on image segmentation and a clinical expertise for the definition of the vessel borders. The main contribution of this paper is a Segmentation-Free Super-Resolution (SFSR) algorithm. Based on inverse problem methodology, SFSR relies on minimizing a compound criterion involving: a data fidelity term, a fluid mechanics term, and a spatial velocity smoothing term. The proposed algorithm is evaluated with respect to state-of-the-art solutions, in terms of quantification error and computation time, on a synthetic 3D dataset with several noise levels, resulting in a 59% RMSE improvement and factor 2 super-resolution with a noise standard deviation of 5% of the Venc. Finally, its performance is demonstrated, with a scale factor of 2 and 3, on a pulsed flow phantom dataset with more complex patterns. The application on *in-vivo* were achievable within the 10 min. computation time.**

***Index Terms*—4D Flow MRI, super-resolution, inverse problems, segmentation-free, spatial regularization**

I. Introduction

BLOOD flow cardiovascular imaging in clinical routine relies mostly on 2D Phase-Contrast MRI. It allows to measure the anatomic shape and the velocity component normal to the 2D acquisition section along the cardiac cycle. A 4D extension of this technique called 4D Flow MRI [1], provides the anatomic shape from the magnitude data and the three velocity components from the phase data within a 3D region of interest and along cardiac cycle. This powerful tool produces a large amount of data which allows to observe complex blood flow patterns and to better understand their underlying effects [2]. Unfortunately, the spatial and time resolutions of 4D Flow MRI data and their signal-to-noise ratio (SNR) are limited due to the constrained clinical acquisition protocol [1], [3]. Both limitations induce significant errors in the quantification of biomarkers of interest such as the wall shear stress (WSS) [4]–[6], the relative pressure [7] and the peak velocity [8]–[10]. Indeed, low resolution and noise affect the assessment of biomarkers involving the computation of spatio-temporal derivatives. In addition, the vessel wall localization using the 4D Flow MRI anatomic signal can be imprecise, and then cause quantification difficulties on wall-related biomarkers. Based on the WSS study [5], an improvement up to 10 % in RMSE has been observed for a resolution difference between 1 mm and 0.7 mm ISO (leading to a scale factor of 1.4). To alleviate theses limitations, this work is focused on resolution enhancement and SNR improvement of 4D Flow MRI data.

Nowadays, Computational Fluid Dynamics (CFD) simulation is considered as a reference approach to assess the blow flow velocity, relative pressure and some fluid mechanic biomarkers on a high resolution mesh [11]. Indeed, velocities, pressure and blood biomarkers are finely described by fluid mechanics laws, and more specifically with the non-linear Navier-Stokes equations. However, CFD simulations rely on a precise definition of the fluid domain and the description of the blood velocity or flow at the inlet. Moreover, measured data and CFD simulation matching can be challenging in clinical routine due to a coarse segmentation or a degraded velocity measurement [11]. To improve that matching, some contributions proposed to learn mechanics laws features from multiple CFD simulations with different inflows or geometries [8], [9], [12]–[15]. Recently, deep learning strategies proposed to enhance the velocity field resolution through synthetic 4D Flow MRI based on CFD simulations [10] and degraded 4D Flow MRI datasets [16]. Similarly to the CFD simulation based approach, the deep learning strategy implies a significant clinical expertise and computation time to built a relevant database.

Besides, other methods used directly the Navier-Stokes equations as in computer vision field [17], [18], or inverse problem theory [19]–[25]. In the first category, measured velocities initiate streamlines, *i.e.* following mechanic laws, which are cleaned to reduce noise influence. In inverse problem theory [26], the problem ill-posedness can be counterbalanced by the addition of prior information, *e.g.* the fluid mechanic laws. For 4D Flow MRI super-resolution (SR), Navier-Stokes (NS) equations are often used as prior information by solving a constrained problem [19]–[23], [25] or through a penalized formulation of the optimized reconstruction [24]. Unfortunately, a pre-established segmentation is a prerequisite in these solutions in order to make the velocity vanishing on the vessel wall. The solution proposed in [24] requires a preliminary step estimating the boundary voxels which are not fully in the fluid or non-fluid domains. Thereby, these

This work was supported in part by Philips Healthcare company under the GIE Grant.

J.M. Serfaty is with Nantes Université, CHU Nantes, CNRS, INSERM, l'Institut du Thorax, F-44000 Nantes, France (JeanMichel.Serfaty@chu-nantes.fr).

S. Levilly and S. Moussaoui are with Nantes Université, École Centrale Nantes, CNRS, LS2N, UMR 6004, F-44000 Nantes, France (sebastien.levilly@ls2n.fr; said.moussaoui@ls2n.fr).

Manuscript received XXX; revised XXX.

boundary voxels are not constrained during the reconstruction to follow the fluid mechanics laws or the no-slip condition. Actually, the segmentation surface and the vessel volume meshing are time consuming steps which also require fluid mechanic expertise and therefore reduce this SR approach applicability in clinical routine. Some recent deep-learning approaches [27], [28] present interesting performance in the segmentation of cardiovascular imaging. Unfortunately, these methods require a large annotated database of 4D flow MRI in different acquisition conditions to fit the clinical routine. These database are not in the public domain and lead to the annotation of images by local experts. Therefore, the application of the trained machine learning to clinical data is not straightforward and may necessitate additional validation steps. In that context, a segmentation-free solution gives the possibility to process dataset by minimizing the clinical expertise time.

The proposed work contribution is focused on the development of a segmentation-free (SF) spatial SR algorithm reducing expert and physician intervention for the SR reconstruction. A previous study [29] introduced an inverse problem based SR algorithm relying on the *a priori* velocity standard deviation and Navier-Stokes equations. Although, it demonstrated interesting performance with segmentation, it became unstable in a SF framework. In the sequel, an extension of that solution is proposed for the stabilization of outflow velocities. More specifically, the optimized criterion, detailed in section II, is made of three parts: a spatially weighted data fidelity term, a penalization term based on Navier-Stokes equations, and a weighted spatial smoothing term promoting steady velocities on low magnetization areas. The latter term is essential to bypass the fluid-domain estimation and therefore allows to set a segmentation-free approach. Besides, the proposed solution is designed to compute each timeframe 3D volume separately on a Graphics Processing Unit (GPU). In section III, three application cases used to validate the proposed algorithm are introduced with a 3D synthetic dataset, a pulsatile flow phantom dataset [30], and a *in-vivo* dataset. These cases were compared to a state-of-the-art solution [19] in terms of quantification error and computation time. In section IV, the proposed method is evaluated with respect to the initial SNR on the 3D synthetic dataset. Then, the performance assessment is completed on a pulsatile flow phantom and clinical dataset with complex flow patterns. Finally, these results are discussed in section V in order to point out applicability conditions and improvement strategies.

II. Methods

A. Problem Formulation

Let's define the vector $\mathcal{Y}$ containing the measured velocity of the 3D volume voxels at a given timeframe. The velocity components $\boldsymbol{u}_\mathrm{d}$, $\boldsymbol{v}_\mathrm{d}$ and $\boldsymbol{w}_\mathrm{d}$ are stacked in the lexicographic order such that $\mathcal{Y} = (\boldsymbol{u}_\mathrm{d}^\mathrm{t}, \boldsymbol{v}_\mathrm{d}^\mathrm{t}, \boldsymbol{w}_\mathrm{d}^\mathrm{t})^\mathrm{t}$ with common a dimension by component of N_d. Specifically, the velocity components vectors have the same dimension $N_\mathrm{d} = N_\mathrm{x} \times N_\mathrm{y} \times N_\mathrm{z}$ where N_x, N_y, and N_z define the field of view dimension. An example of the data velocity vectors is illustrated by blue component-wise vectors in the Figure 1.

Then, we define the velocity component vectors $\boldsymbol{u}$, $\boldsymbol{v}$, and $\boldsymbol{w}$ and the pressure field $\boldsymbol{p}$ which contain the 3D volume voxel values at the super-resolved grid resolution. The resulting dimension of $\boldsymbol{u}$, $\boldsymbol{v}$, $\boldsymbol{w}$, and $\boldsymbol{p}$ depend on the SR scale factor s such that, for a staggered grid as depicted in Figure 1, $N_{\boldsymbol{u}} = \mathrm{s}^3(N_\mathrm{x}-1)N_\mathrm{y}N_\mathrm{z}$, $N_{\boldsymbol{v}} = \mathrm{s}^3N_\mathrm{x}(N_\mathrm{y}-1)N_\mathrm{z}$, $N_{\boldsymbol{w}} = \mathrm{s}^3N_\mathrm{x}N_\mathrm{y}(N_\mathrm{z}-1)$, and $N_{\boldsymbol{p}} = \mathrm{s}^3N_\mathrm{x}N_\mathrm{y}N_\mathrm{z}$. Each of these components are organized in the lexicographic order. Then, we define the vector $\mathcal{X}$ such that $\mathcal{X} = (\boldsymbol{u}^\mathrm{t}, \boldsymbol{v}^\mathrm{t}, \boldsymbol{w}^\mathrm{t}, \boldsymbol{p}^\mathrm{t})^\mathrm{t}$. The proposed solution, called SFSR for Segmentation-Free Super-Resolution, is based on solving the following criterion minimization problem:

$$\hat{\mathcal{X}} = \underset{\mathcal{X}\in\mathbb{R}^N}{\arg\min}\ \mathcal{F}(\mathcal{X},\mathcal{Y}) + \alpha\mathcal{NS}(\mathcal{X}) + \beta\mathcal{R}(\mathcal{X}) \qquad (1)$$

where $N = N_{\boldsymbol{u}} + N_{\boldsymbol{v}} + N_{\boldsymbol{w}} + N_{\boldsymbol{p}}$ is the $\mathcal{X}$ vector size, $\mathcal{F}$ is the data fidelity term, $\mathcal{NS}$ is a regularization term using the non-linear Navier-Stokes equations, and $\mathcal{R}$ is a velocity smoothing term. These three ℓ_2-norm criteria are detailed in the following sections. The regularization terms are weighted by two scalar parameters α and β.

B. Data Fidelity Term

As in [20], the data fidelity term involves the velocity components discrepancy only. Although other contributions like [24] preferred a more native writing through a complex formulation, the proposed solution uses the *a priori* velocity standard deviation as a weight to account for the magnetization relationship with velocity error. Specifically, the criterion $\mathcal{F}$ can be written as:

$$\mathcal{F}(\mathcal{X},\mathcal{Y}) = \|\mathcal{Y} - \mathbf{H}\mathcal{X}\|^2_{\mathbf{W}} \qquad (2)$$

where $\mathbf{W}$ is a diagonal weight matrix of *a priori* velocity variances [3], and $\mathbf{H}$ is the downsampling and filtering operator [19], [20], [24] as depicted in Fig. 1. Besides, the simplified forward model, modeled by the matrix $\mathbf{H}$, considers real-valued images instead of complex-valued ones in order to remove the magnetization from the SR reconstruction.

Let's highlight that super-resolution model simplification is motivated by its applicability to images provided by multiple clinical devices without the need to process the k-space data. Moreover, a very precise model is not straightforward to apply for MRI data obtained by accelerated or compressed sensing strategies since the theoretical Point-Spread-Function (PSF) is obtained under the hypothesis of fully sampled k-space. Actually, this hypothesis has been successfully used in several super-resolution algorithms [19], [20]. It also reduces significantly the computation time and allows to reach a satisfying performance level. For the sake of simplicity, the current study has been led with a mean filter as in [30], and could be extended to a cardinal sine kernel [19], or any appropriate other kernel. More details about the operator $\mathbf{H}$ design and implementation are given in the appendix A.

Each velocity component being encoded in the phase of the measured signal, the velocity measurement error is not identically distributed but spatially variant [3]. Particularly, the error is higher in low magnetization areas, *i.e.* outside

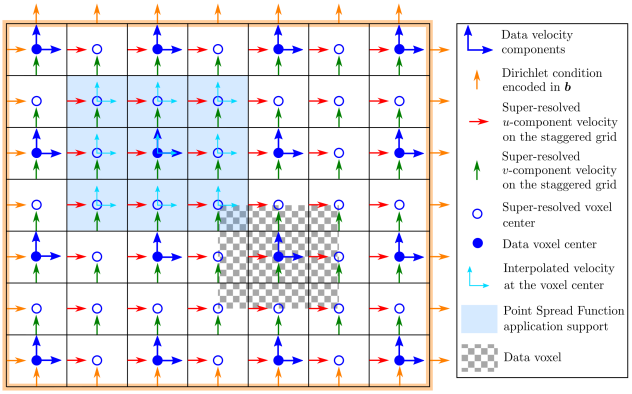

Fig. 1. Downsampling and filtering operator schematic description with the (u, v) velocity represented on the staggered grid.

of potential fluid flow domain, as expressed by the *a priori* standard deviation value [3]:

$$\sigma_{\mathrm{v},i} = \frac{\sqrt{2}}{\pi} \frac{V_{\mathrm{enc}}}{\mathrm{SNR}_i} \tag{3}$$

where V_{enc} designates the encoding velocity, and SNR_i the signal-to-noise ratio of the anatomical signal in the i-th voxel. Then, the weight matrix appearing in the least squares data fitting term $\mathcal{F}$ is then defined by $\mathbf{W} = \mathrm{diag}\left\{\frac{1}{2\sigma^2_{\mathrm{v},i}}\right\}_{i=1\cdots N_\mathrm{d}}$, with N_d the data size. It can be noted that this weighting scheme reduces the data influence on the solution outside the expected fluid domain.

C. Fluid Mechanic Term

In most CFD simulations [11], [30] and for 4D flow MRI SR applications [19], [20], [24], the blood is assumed to be incompressible and homogeneous. Thus, the fluid density ρ and dynamic viscosity μ are assumed to be time and spatially invariant.

In such flows, the velocity at each position, is expressed by its components (u, v, w), which are governed by mass and momentum conservation equations, also called the incompressible Navier-Stokes equations:

$$u_\mathrm{x} + v_\mathrm{y} + w_\mathrm{z} = 0 \tag{4}$$

$$\rho(uu_\mathrm{x} + vu_\mathrm{y} + wu_\mathrm{z}) + p_\mathrm{x} - \mu(u_\mathrm{xx} + u_\mathrm{yy} + u_\mathrm{zz}) = 0 \tag{5}$$

$$\rho(uv_\mathrm{x} + vv_\mathrm{y} + wv_\mathrm{z}) + p_\mathrm{y} - \mu(v_\mathrm{xx} + v_\mathrm{yy} + v_\mathrm{zz}) = 0 \tag{6}$$

$$\rho(uw_\mathrm{x} + vw_\mathrm{y} + ww_\mathrm{z}) + p_\mathrm{z} - \mu(w_\mathrm{xx} + w_\mathrm{yy} + w_\mathrm{zz}) = 0 \tag{7}$$

where p denotes the blood pressure and the use of the subscript $(\cdot)_l$ implies the derivative in the l-direction. For instance, u_x stands for the derivative of the u-velocity component in the direction x, and u_xy for the second order derivative along y and x directions.

In our approach, body forces and transient velocity terms are voluntarily ignored in order to get a time-independent design which facilitate computational parallelization in time. The underlying effect of that assumption will be discussed in section IV-B on the pulsatile Phantom application case. Consequently, the problem (1) can be solved for each cardiac phase separately.

The Navier-Stokes equations are applied on the whole super-resolved 3D volume and Dirichlet conditions are set for velocities on the borders of that volume, as depicted in Fig. 1 in orange. By default, the borders velocities are fixed by linear interpolation of the measured 4D Flow MRI data. However, if no flow cross a specific border, a no-slip condition can be enforced, *i.e.* $u = v = w = 0$. Partial Derivative Equations (4), (5), (6), and (7) are discretized by a finite-volume method (FVM) involving the upwind integration scheme [19], [31], [32]. In FVM , estimated velocities are localized on the borders of each cell. In this work, the super-resolved voxels are considered as cells which led us to use a staggered grid [31], [32] as depicted in Fig. 1 by a blue circle for the cell center and by red and green vectors for each velocity component. Equations (4), (5), (6), and (7) are integrated over the super-resolved voxels which led to their linearization in the vicinity of any velocity state $\mathcal{X}_k$. The subscript k stands for the iteration k of the super-resolved velocity field. Consequently, the regularization term $\mathcal{NS}(\mathcal{X})$ becomes the squared L2 norm of the linearized mass and momentum conservation equations such as:

$$\mathcal{NS}_k(\mathcal{X}) = \|\mathbf{S}_{\mathcal{X}_k}\mathcal{X} - \boldsymbol{b}\|_2^2 \tag{8}$$

where $\mathbf{S}_{\mathcal{X}_k}$ is the convection-diffusion matrix computed from $\mathcal{X}_k$ and $\boldsymbol{b}$ contains the boundary conditions. Using matrix $\mathbf{S}_{\mathcal{X}_k}$ is consistent with coupled velocity-pressure solving, in opposition to the segregated scheme adopted by Rispoli *et al.* [19]. For more details on the construction of $\mathbf{S}_{\mathcal{X}_k}$, an exhaustive introduction of finite-volume method can be found in Chapters 5 and 6 of [31], and Chapter 4 of [32]. In addition, the appendix B presents briefly the Navier-Stokes equations integration by FVM.

Numerically, the operation $\mathbf{S}_{\mathcal{X}_k}\mathcal{X}$ is a kernel-variant convolution of the current velocity $\mathcal{X}$ with the finite-volume coefficients associated with each voxel faces, *i.e.* connecting with 6 neighbours. In terms of implementation, $\mathbf{S}_{\mathcal{X}_k}$ being extremely sparse, the proposed solution does not create the matrix itself but only its coefficients. Consequently, the $\mathbf{S}_{\mathcal{X}_k}$ operator applies element-wise multiplication and summation which are particularly suitable for GPU computation.

D. Velocity Smoothing Term

In our previous study [29], a solution based on a two terms criterion, *i.e.* a data fidelity term and fluid mechanic term, demonstrated its efficiency to enhance the resolution when the fluid domain segmentation is known. However, its application in a SF framework showed instabilities and degradation in the interface in/out fluid due to the velocities estimated outside the potential fluid domain area. Indeed, these velocities were mainly influenced by the fluid mechanic term, since the weight on the data is lower and no fluid borders is encoded within the boundary variable $\boldsymbol{b}$ appearing in the term $\mathcal{NS}_k(\mathcal{X})$.

To alleviate this effect, the proposed solution regularize the spatial evolution of velocity components and particularly

in low magnetization areas. The regularization term $\mathcal{R}$ is therefore defined as:

$$\mathcal{R}(\mathcal{X}) = \|\mathbf{G}_{\mathrm{x}}\mathcal{X}\|^2_{\overline{\mathbf{W}}} + \|\mathbf{G}_{\mathrm{y}}\mathcal{X}\|^2_{\overline{\mathbf{W}}} + \|\mathbf{G}_{\mathrm{z}}\mathcal{X}\|^2_{\overline{\mathbf{W}}} \quad (9)$$

$$= \mathcal{X}^{\mathrm{t}}\mathbf{M}\mathcal{X} \quad (10)$$

with $\mathbf{M} = \mathbf{G}_{\mathrm{x}}^{\mathrm{t}}\overline{\mathbf{W}}\mathbf{G}_{\mathrm{x}} + \mathbf{G}_{\mathrm{y}}^{\mathrm{t}}\overline{\mathbf{W}}\mathbf{G}_{\mathrm{y}} + \mathbf{G}_{\mathrm{z}}^{\mathrm{t}}\overline{\mathbf{W}}\mathbf{G}_{\mathrm{z}}$ where $\mathbf{G}_{\mathrm{x}}$, $\mathbf{G}_{\mathrm{y}}$ and $\mathbf{G}_{\mathrm{z}}$ are finite-difference matrices along each space direction, and $\overline{\mathbf{W}}$ is a diagonal matrix filled with the *a priori* standard deviation such as $\overline{\mathbf{W}} = \mathrm{diag}\left\{2\sigma_{\mathrm{v}_i}^2\right\}_{i=1\cdots N}$. That super-resolved *a priori* standard deviation is computed from (3) with the anatomic SNR being estimated thanks to the tri-linear interpolation of the magnetization [33]. Thus, outer velocities are significantly smoothed by both $\mathcal{NS}$ and $\mathcal{R}$ terms. Meanwhile, the fluid domain velocities are mainly regularized by Navier-Stokes equations and softened to a lesser extent by $\mathcal{R}$.

E. Optimization Algorithm

Thanks to the first order approximation induced by the finite-volume integration of the fluid mechanic term, the non-linear problem (1) can be reformulated at each iteration as the solving of a linear weighted least-squares problem in the vicinity of any $\mathcal{X}_k$:

$$\min_{\mathcal{X}\in\mathrm{R}^N} \|\mathcal{Y} - \mathbf{H}\mathcal{X}\|^2_{\mathbf{W}} + \alpha\,\|\mathbf{S}_{\mathcal{X}_k}\mathcal{X} - \boldsymbol{b}\|_2^2 + \beta\,\mathcal{X}^{\mathrm{t}}\mathbf{M}\mathcal{X} \quad (11)$$

whose solution $\hat{\mathcal{X}}$ is obtained by solving the following linear system:

$$\left(\mathbf{H}^{\mathrm{t}}\mathbf{W}\mathbf{H} + \alpha\,\mathbf{S}_{\mathcal{X}_k}^{\mathrm{t}}\mathbf{S}_{\mathcal{X}_k} + \beta\,\mathbf{M}\right)\mathcal{X} = \left(\mathbf{H}^{\mathrm{t}}\mathbf{W}\mathcal{Y} + \alpha\,\mathbf{S}_{\mathcal{X}_k}^{\mathrm{t}}\boldsymbol{b}\right) \quad (12)$$

using a preconditioned linear conjugate gradient (PLCG) algorithm. This iterative resolution scheme efficiency is optimized thanks to the construction of dedicated operators instead of large sparse matrices for $\mathbf{H}$, $\mathbf{S}_{\mathcal{X}_k}$, $\mathbf{M}$, and $\mathbf{W}$. Furthermore, the extensive use of GPU (Nvidia RTX A4000, 8 Gb) and RAM (64 Gb) helped reducing the computation time. The non-linear optimization algorithm is assumed to be converged once the normalized evolution of $\hat{\mathcal{X}}$ between two successive iterations, $\|\hat{\mathcal{X}}_k - \hat{\mathcal{X}}_{k-1}\|_2^2 / \|\hat{\mathcal{X}}_{k-1}\|_2^2$, reaches a tolerance threshold ($\epsilon_x = 10^{-6}$). This non-linear optimization problem solving procedure is summarized in the Algorithm 1. This algorithm has been already tested on 2D synthetic and phantom datasets relying on steady fluid flows [34]. Even if the unsteady term in the Navier-Stokes equation is neglected, we will demonstrate the effectiveness of this algorithm on a fluid with pulsatile flow and 3D complex flow patterns. The whole pipeline of the proposed solution is illustrated in Fig. 2.

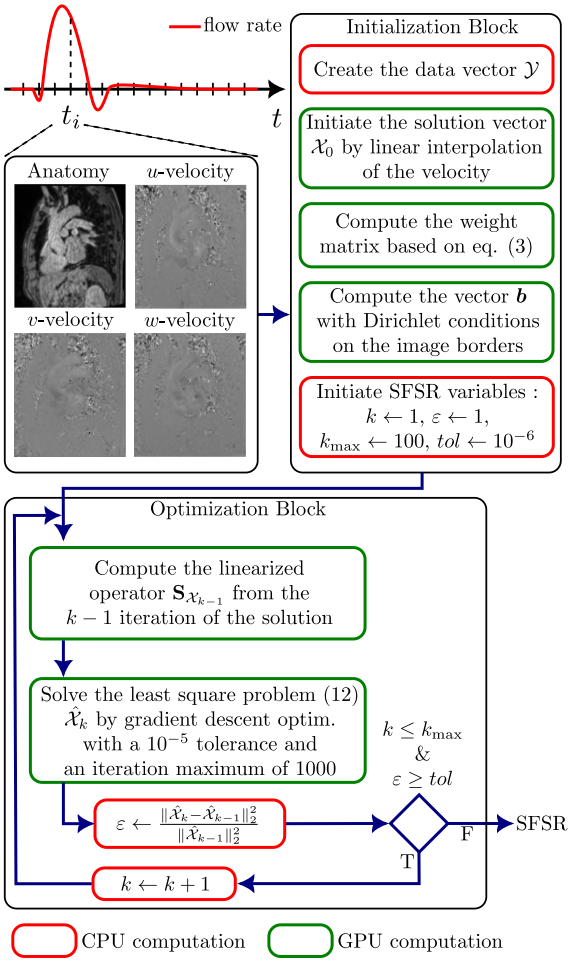

Fig. 2. Illustration of the proposed SFSR solution pipeline.

Algorithm 1 SFSR Algorithm applied on a 3D volume at a given cardiac phase

$\mathcal{Y} \leftarrow (\boldsymbol{u}_{\mathrm{d}}^{\mathrm{t}}, \boldsymbol{v}_{\mathrm{d}}^{\mathrm{t}}, \boldsymbol{w}_{\mathrm{d}}^{\mathrm{t}})^{\mathrm{t}}$ % contains the measured velocities
$\mathcal{X}_0 \leftarrow (\boldsymbol{u}_0^{\mathrm{t}}, \boldsymbol{v}_0^{\mathrm{t}}, \boldsymbol{w}_0^{\mathrm{t}}, \boldsymbol{p}_0^{\mathrm{t}})^{\mathrm{t}}$ % filled by tri-linear interpolation of $\mathcal{Y}$ on the SR grid and $\boldsymbol{p}_0$ is set to zero
$\mathbf{W}$ % data weight matrix from equation (3)
$\boldsymbol{b}$ % contains Dirichlet conditions on image borders
$k \leftarrow 1$; $\varepsilon \leftarrow 1$; $k_{\max} \leftarrow 100$; $tol \leftarrow 10^{-6}$
while ($k \le k_{\max}$ and $\varepsilon \ge tol$) **do**
  $\mathbf{S}_{\mathcal{X}_{k-1}}$ % computed by FVM on velocity $\hat{\mathcal{X}}_{k-1}$
  $\hat{\mathcal{X}}_k$ % obtained by solving the linear problem (12) using PLCG optimization
  $\varepsilon \leftarrow \|\hat{\mathcal{X}}_k - \hat{\mathcal{X}}_{k-1}\|_2^2 / \|\hat{\mathcal{X}}_{k-1}\|_2^2$ % stopping rule test
  $k \leftarrow k+1$
end while

III. Validation Protocol

This section aims to introduce the three applications with synthetic, phantom, *in-vivo* datasets with respectively a steady flow, *i.e.* Poiseuille flow, a pulsatile flow with complex flow patterns, and a cardio-thoracic 4D Flow MRI acquisition. Then, we assess the performance of the proposed SFSR algorithm by comparing the indicators defined in section III-D with three state-of-the-art solutions:

- the algorithm introduced in [19], called SbSR for SIMPLER-based Super-Resolution, which relies on a constrained formulation for the mass conservation equation, and a pre-established segmentation.
- a previous study [29], called PSR for Penalized Super-Resolution, which is based on a two-fold penalized criterion with a data fidelity term and a fluid mechanic term, and the *a priori* knowledge of the fluid domain.
- a naive option to increase spatial resolution is the linear

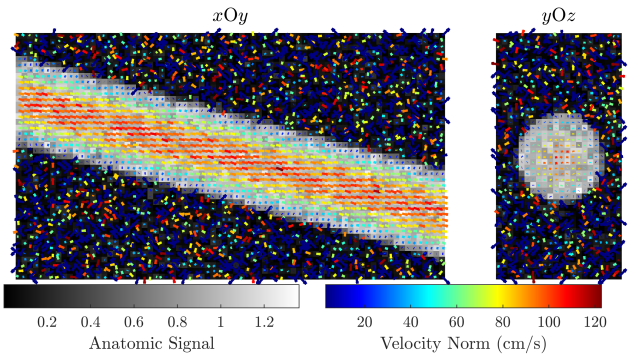

Fig. 3. 3D Synthetic dataset based on Poiseuille Flow.

interpolation of the velocity field, *i.e.* called LISR. For sake of balance, the SbSR and PSR algorithms have been also implemented in order to use the full potential of GPU computation. Finally, we introduce the methodology to determine the hyper-parameters in section III-E.

A. Synthetic Dataset

A synthetic dataset has been designed in order to control the noise level in the data and to discuss its impact on the algorithm performance. The field of view in this dataset is set to $15\ \mathrm{cm} \times 8.6\ \mathrm{cm} \times 4.4\ \mathrm{cm}$ and divided between two regions: a non-fluid area where the magnetization is low in opposition to an other one with fluid circulation and high magnetization. Fig. 3 illustrates these two regions with a 2D section of the magnetization in gray-scale and velocity norm in color-scale. The fluid domain is defined as a straight $15°$-tilted tube with a radius of $1.5\ \mathrm{cm}$ leading to a parabolic velocity field, called Poiseuille, with a top value of $1\ \mathrm{m/s}$. The synthetic fluid model uses a dynamic viscosity μ of $0.0032\ \mathrm{Pa.s}$ and a fluid density ρ of $1060\ \mathrm{kg/m^3}$. A high resolution reference velocity field, set to an isotropic (ISO) spatial resolution of $1\ \mathrm{mm}$, is obtained by computing the analytical solution of the Poiseuille flow. The latter is used as a phase in a complex-valued magnetization which is then filtered by a $7 \times 7 \times 7$ *sinc*-kernel function introducing partial volume effect and leading to a synthetic 4D Flow MRI dataset with a spatial resolution of $2\ \mathrm{mm}$. A zero-mean complex-valued Gaussian noise is added and the velocity is consequently extracted from the resulting phase.

For the sake of simplicity, the resulting velocity noise standard deviation will refer to a percentage of the V_{enc} in the fluid domain (which is defined as $120\,\%$ of the maximum theoretical velocity). According to [5], [35], a percentage of $5\,\%$ corresponds to the highest noise level encountered with a $1.5\ \mathrm{T}$ MRI (no contrast enhancement). In order to represent highly degraded acquisitions, SFSR is evaluated with four values of V_{enc} percentage: $2.5\,\%$, $5\,\%$, $7.5\,\%$ and $10\,\%$

B. Phantom Dataset

This study uses the phantom dataset developed by Puiseux *et al.* [30]. Its geometry is consistent with cardiovascular vessel shapes with an arch of $26\ \mathrm{mm}$ diameter and a central connection with a swelling representing an aneurysm. That configuration helps measuring complex flow patterns within a pulsatile flow context. Puiseux *et al.* acquisition were performed on a $1.5\ \mathrm{T}$ MRI (Siemens Magnetom Avantado, Siemens Medical Systems, Erlangen, Germany) with prospective gated. Here, only the isotropic $2\ \mathrm{mm}$ resolution dataset is used with a V_{enc} of $0.5\ \mathrm{m/s}$ in the three directions.

In addition, this phantom dataset and the super-resolved solutions were compared to a CFD simulation, using the YALESBIO solver [36]. It exploits a Large-Eddy-Simulation strategy in order to better represent small scale turbulent flow. Specifically, the CFD simulation mesh is made of cells with a characteristic size of 0.7 mm. The cinematic viscosity ν and the fluid density ρ are set to $4.02 \times 10^{-6}\ \mathrm{m^2/s}$ and $1020\ \mathrm{kg/m^3}$. The CFD simulated velocity was phase-averaged in order to be consistent with the 4D flow MRI acquisition which measures over multiple cardiac cycle. More details about the experimental setup and the CFD simulation can be found in the full paper study [30].

C. In-vivo dataset

The *in-vivo* dataset presented in section IV-C has been measured on a healthy volunteer with a 4D flow MRI sequence from the $1.5\ \mathrm{T}$ MRI system (Siemens Aera, Siemens Medical Systems, Erlangen, Germany). The research was carried out following the principles of the Declaration of Helsinki. The echo and repetition times were set respectively to $2.22\ \mathrm{ms}$ and $38.16\ \mathrm{ms}$ with a flip angle of $15°$. The voxel image resolution is set to $2.2\ \mathrm{mm} \times 2.2\ \mathrm{mm} \times 2\ \mathrm{mm}$ with a velocity encoding V_{enc} of $200\ \mathrm{cm/s}$. The full matrix acquisition has a size of $[144, 130, 40, 30]$ to account for the thoracic volume over the cardiac cycle. For a sake of efficiency, the SFSR algorithm has been applied on a reduced matrix of dimension $[71, 91, 40, 30]$ which focus on the main circulatory area: heart and aorta. Besides, hemodynamic parameters ρ and ν were respectively set to $1060\ \mathrm{kg/m^3}$ and $0.0034\ \mathrm{Pa.s}$. Finally, the background phase error were corrected in order to avoid any smooth bias within the fluid domain [37].

D. Performance Indicators

The retained performance indicators are the Root-Mean-Square-Error (RMSE), Pearson's correlation, and computation time. Each SR reconstruction algorithm performance indicator is evaluated by considering the theoretical or the numerically computed velocity field as a reference. Most hemodynamic biomarkers rely on the velocity within the vessel, and consequently the performance indicators are restricted to the fluid domain. The RMSE is defined as:

$$\mathrm{RMSE}(\boldsymbol{r}) = \sqrt{\Sigma_{i=1}^{N} (\boldsymbol{r}_i - \overline{\boldsymbol{r}}_i)^2 / N} \tag{13}$$

where $\overline{\boldsymbol{r}}$ contains the super-resolved reference velocity field. In order to quantify the improvement, let's define the normalized Root-Mean-Square Error, denoted by nRMSE, as the RMSE divided by data $\mathrm{RMSE_d}$ which is equal to $\sqrt{\frac{1}{N_{\mathrm{d}}} \sum_{i=1}^{N_{\mathrm{d}}} \left(\mathcal{Y}_i - \overline{\mathcal{Y}}_i\right)^2}$ with $\overline{\mathcal{Y}}$ for the low resolution unfiltered reference velocity field.

Finally, we have also calculated the Pearson correlation value r between the estimated velocity magnitudes $\boldsymbol{c}$ and their respective reference ones $\boldsymbol{c}^*$:

$$r_{\boldsymbol{c}} = \left(\sum_{j=1}^{N} \nu_j \nu_j^*\right) \left(\sum_{j=1}^{N} \nu_j^2 \sum_{j=1}^{N} (\nu_j^*)^2\right)^{-1/2} \quad (14)$$

where ν_j and ν_j^* are statistically centered velocity magnitudes.

E. Hyper-parameter setting

The proposed method SFSR and its related criterion depend on two types of parameters: the penalization weights (α, β) and the hemodynamic parameters (ρ, μ). The aim of this section is to demonstrate the existence of optimal values of these parameters that improve the RMSE. We highlight that the unsupervised tuning of these parameters would require further developments that are not discussed in this paper.

The coefficients α and β control respectively the weight of the fluid mechanic regularization and the spatial smoothing whereas ρ and μ define the hemodynamic fluid regime in the Navier-Stokes model. The penalization weights have been set in a way to minimize the RMSE in each configuration. For instance, Fig. 4(a), shows the evolution of the RMSE with respect to α and β for the Phantom dataset (a 13x25 grid search takes about 12 h). One can see that retaining non-zero values for both parameters lead to RMSE decrease. Moreover, it can be noted that an adequate parameter values can be found to balance the two regularization terms (Navier-Stokes and Smoothing) and lead to a significant decrease of the nRMSE. Indeed, the fluid mechanic regularization fully benefit to the solution only when the spatial smoothing is sufficient to discriminate flow and no-flow areas.

An analysis of the influence of the hemodynamic parameters on the proposed algorithm performance was conducted with consistent range values provided by [38] for the dynamic viscosity and by [39] for the blood density. These parameters define the blood flow regime through the Reynolds number representing the ratio between the inertial and viscous forces. Although the variation of the hemodynamic parameters on the studied range values induces a Reynolds number change up to a 3.5 factor, these parameters impact is negligible in term of nRMSE with a standard deviation of 0.41 %. Besides, the SFSR criterion convergence is shown in Fig. 4(b) for each application case. One can see that only few iterations are needed before reaching algorithm convergence.

IV. Results

Three kinds of performance analysis are presented in this section. First, both SR solutions are applied to a synthetic dataset with different noise levels. Then, SR applicability is demonstrated on a pulsatile phantom dataset with complex flow patterns. Finally, we will observe the SR improvement on a *in-vivo* dataset and focus on specific regions of interest.

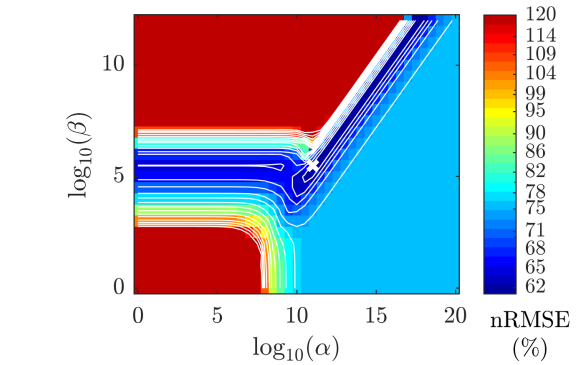

(a) Penalization weights influence on SFSR nRMSE (limited to 120 %)

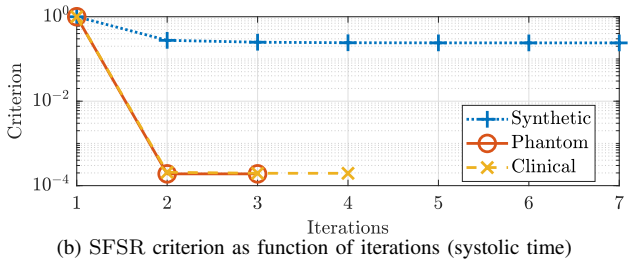

(b) SFSR criterion as function of iterations (systolic time)

Fig. 4. Hyper-parameters influence on SFSR RMSE on the Phantom dataset at the systolic time and illustration of the SFSR criterion decrease.

A. Performance Analysis on a Simulated Dataset

In 4D Flow MRI, SNR is the result of a compromise with two other factors: the spatio-temporal resolution and the acquisition time. According to [35], the maximum σ_{v} encountered in clinical routine is about 5 % of the V_{enc}. To account for particularly noisy data, obtained with higher acceleration factor for instance, four noise standard deviations were tested with 2.5, 5, 7.5, and 10 % of the V_{enc}. Table I shows the average and the standard deviation of the performance indicators over 20 noise realizations. The results gather the performance of three state-of-the art approaches and the proposed SFSR solution with a SR factor of 2 on the synthetic dataset, *i.e.* a resolution enhancement from 2 mm ISO to 1 mm ISO.

In terms of quantification, SFSR leads to better performance than SbSR with a RMSE improvement ratio between 2 and 3.6. According to the SbSR nRMSE indicator, the SR reconstruction is beneficial only for a $\sigma_{\text{v}} \geq 5$ % of the V_{enc}. The SbSR nRMSE for the 2.5 and 5 % noise cases is above 100 % which means here that the error level is 113.8 and 10.1 % higher after super-resolution than in the initial dataset. Meanwhile, SFSR solution is able to reduce the nRMSE to 58.6 % even in low noise cases, *i.e.* representing an error reduction of at least 41.4 %. One can notice the increase of the RMSE for the PSR, LISR, and SFSR methods along with the noise standard deviation. In case of a standard deviation exceeding 5 % of the V_{enc}, PSR algorithm RMSE is degrading faster than SFSR and slower than LISR.

Besides, the Pearson's correlation between SbSR solution and the reference velocity magnitudes are higher than 87.9 % in all cases while SFSR outperforms with values exceeding 99.4 %. In addition, SFSR is more efficient for a larger range of standard deviation σ_{v} in comparison to PSR correlation which slightly decrease. Moreover, LISR correlation is even

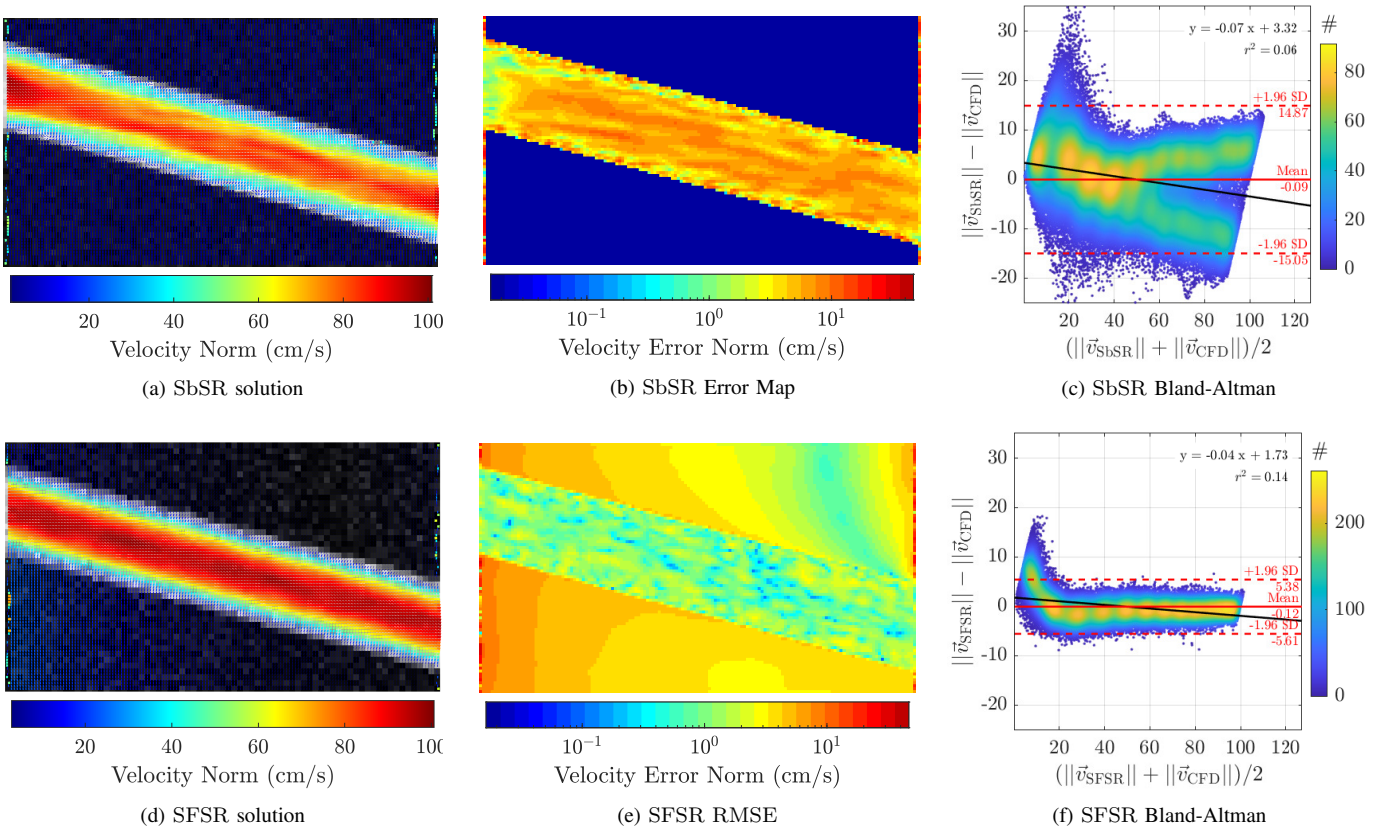

(a) SbSR solution (b) SbSR Error Map (c) SbSR Bland-Altman

(d) SFSR solution (e) SFSR RMSE (f) SFSR Bland-Altman

Fig. 5. SFSR and SbSR solutions along with their respective error maps and Bland-Altman graphs represented in the xOy plane. The SR algorithms enhance the synthetic dataset resolution from 2 mm ISO to 1 mm ISO.

σ_v	2.5 %×V_{enc}	5 %×V_{enc}	7.5 %×V_{enc}	10 %×V_{enc}
Method	RMSE (cm/s)			
SbSR	9.7 (0.21)	9.2 (0.21)	8.9 (0.29)	16.5 (1.51)
PSR	3.5 (0.10)	5.5 (**0.04**)	7.7 (0.13)	10.1 (0.18)
LISR	3.9 (0.02)	6.6 (**0.04**)	9.5 (0.06)	12.6 (0.08)
SFSR	**3.2** (**0.01**)	**3.4** (0.08)	**4.4** (**0.03**)	**4.5** (**0.05**)
Method	nRMSE (%)			
SbSR	213.8 (4.9)	110.1 (2.6)	71.0 (2.3)	96.3 (8.6)
PSR	75.9 (2.2)	65.0 (0.4)	61.3 (1.0)	58.6 (1.0)
LISR	85.4 (0.4)	78.7 (**0.3**)	75.9 (0.3)	73.5 (**0.3**)
SFSR	**69.8** (**0.3**)	**41.0** (1.0)	**34.8** (**0.2**)	**26.0** (**0.3**)
Method	Pearson's correlation (%)			
SbSR	95.8 (0.268)	96.7 (0.236)	96.7 (0.336)	87.9 (2.295)
PSR	**99.6** (0.027)	99.1 (**0.015**)	98.3 (0.079)	97.2 (0.146)
LISR	99.5 (0.007)	98.6 (0.022)	97.2 (0.049)	95.1 (0.102)
SFSR	**99.6** (**0.004**)	**99.6** (0.039)	**99.4** (**0.012**)	**99.4** (**0.020**)
Method	Computation Time (s)			
SbSR	2136 (342)	2750 (114)	1573 (229)	1290 (903)
PSR	581 (465)	493 (346)	516 (338)	665 (385)
LISR	**0.03** (**0.007**)	**0.03** (**0.004**)	**0.03** (**0.004**)	**0.03** (**0.004**)
SFSR	154 (5)	648 (134)	63 (3)	565 (55)

TABLE I
PERFORMANCE INDICATORS OF BOTH SR SOLUTIONS FOR DIFFERENT NOISE LEVELS. EACH VALUE IS THE MEAN PERFORMANCE INDICATOR OVER 20 REALIZATIONS WITH THEIR RESPECTIVE STANDARD DEVIATION BETWEEN BRACKETS.

more impacted in case of high noise. Finally, the computation time is clearly in favour of the LISR method. Unfortunately, this option has poor quantification performance and naturally, SFSR approach becomes the best solution in term of computation time and quantification performance. One can notice the acceleration factor of SFSR between 2.3 and 25 in comparison to SbSR. Let's notice that the computation time standard deviations are also significantly lower for the SFSR approach.

These performance indicators represent the quantification error over the whole fluid domain and need to be completed by local observations. Fig. 5 illustrates the SR results of SbSR and SFSR applied to a synthetic dataset with a standard deviation of 5 % of the V_{enc}, along with their voxel-wise RMSE maps and Bland-Altman graphs on velocity magnitudes. One can notice the strict nullity of velocities outside the fluid domain for SbSR in Fig.5(a) while SFSR ones are following a smooth gradient in Fig.5(d). Error maps for both solutions are represented by Fig. 5(b) and 5(e) for SbSR and SFSR respectively. As depicted in the velocity field figures, the error maps outside the fluid domain is much higher for SFSR than SbSR. However, SFSR performs particularly well in the region of interest, *i.e.* the fluid domain. Fig. 5(c) and 5(f) shows the Bland-Altman graphs of SbSR and SFSR respectively between the solutions' velocity magnitudes and the reference ones. SbSR error discrepancy is smaller for low magnitudes velocities, *i.e.* near wall velocities, and its error increase significantly as function of the magnitude. Meanwhile, SFSR performs better in higher velocities with a confidence interval 2.7 times smaller than SbSR. As expected from the design of SFSR, which does not enforce the no-slip condition on the fluid domain borders, the velocity is slightly overestimated near the vessel wall (but in an order

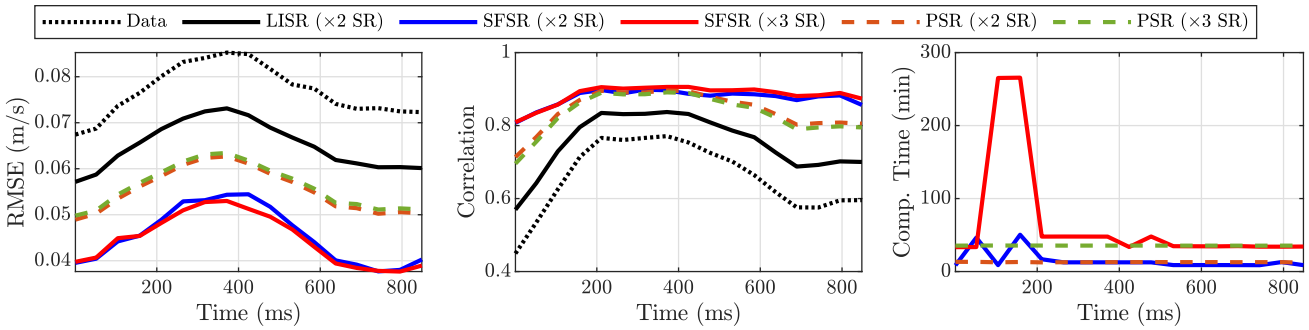

Fig. 6. Performance indicators during the cardiac cycle.The 4D Flow MRI has a spatial resolution of 2 mm ISO. A SR factor of 2 and 3 lead respectively to an effective resolution 1 mm ISO and 0.66 mm.

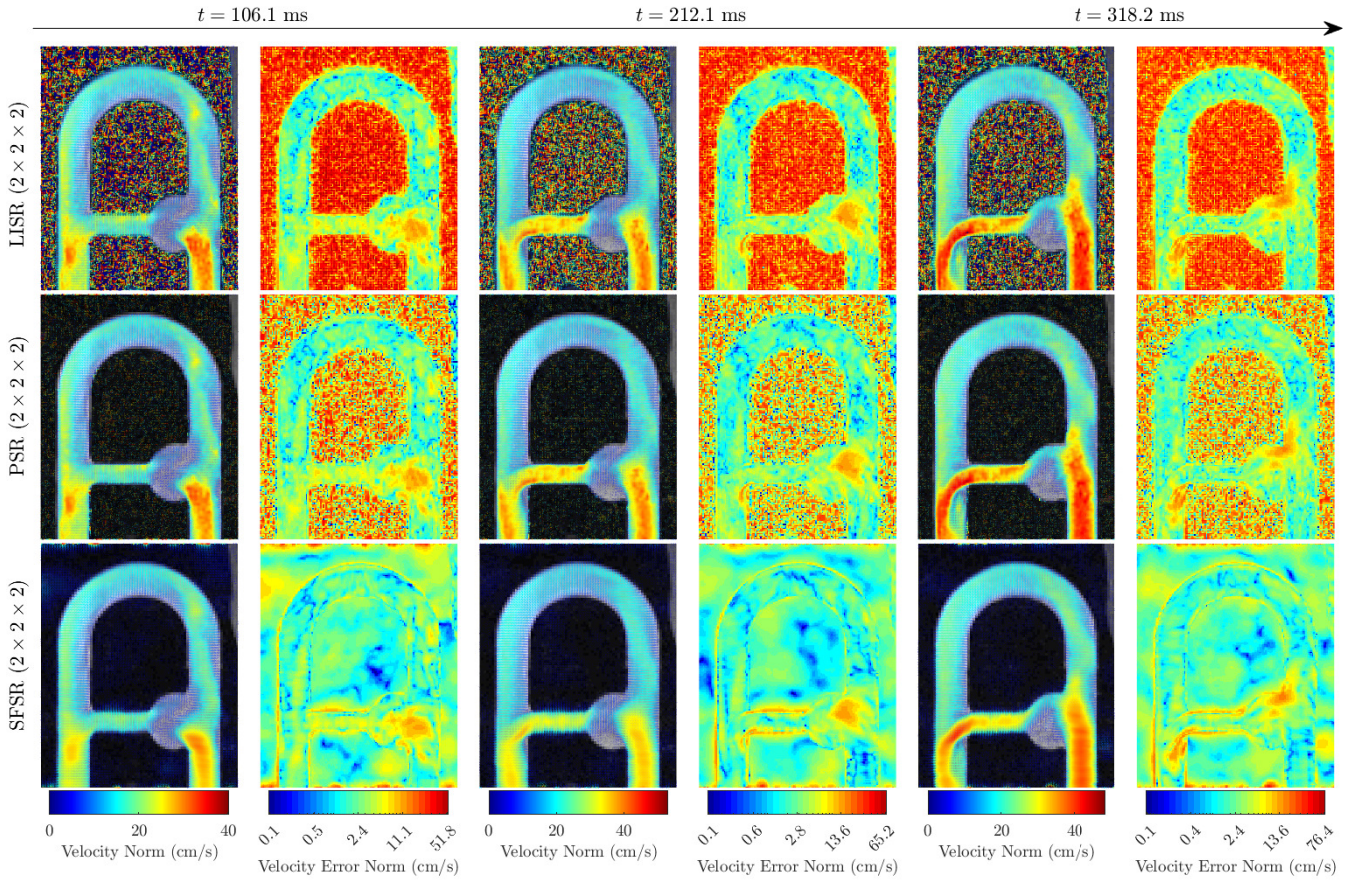

Fig. 7. LISR, PSR, and SFSR super-resolved velocity (1 mm ISO) and error maps during the cardiac cycle. The colored bars of the error maps are represented using a logarithmic scale to clearly indicate the most complex regions to process.

of magnitude smaller than the SbSR approach).

As a consequence of these observations, the SbSR solution is no longer considered in the following analysis, in particular because of its high computation time and the challenge of converging the solution.

B. Evaluation on a Pulsatile Flow Phantom Dataset

In cardiovascular imaging, lower limb blood flow can be modeled by a Poiseuille flow since the pulse is significantly reduced. But, the aorta blood flow is much more complex due to its particular shape and to its pulsatile nature. The proposed solution is tested on the Phantom dataset developed by Puiseux *et al.* [30] which has most of the complexity observed in the aorta with a U-tube representing an arch and a swelling inducing complex flow similarly to aneurysm. Akin to the previous analysis, SFSR algorithm is evaluated by assessing its performance indicators within the blood flow domain. The observation of error maps over different phases of the cardiac cycle provide insight about the complex regions to solve.

Fig. 6 shows the RMSE, Pearson's correlation and computation time over the 17 phases. These indicators are calculated for the 4D Flow MRI dataset, LISR, and the SFSR and PSR reconstructions for two SR factor: 2 and 3 by dimension. Due to the resolution of the 4D Flow MRI (2 mm ISO), the resulting SR resolution is 1 mm ISO for the factor

2 SR and 0.66 mm ISO for the SR factor 3. The CFD reference resolution being of 0.7 mm, we did not considered higher SR factors. In term of RMSE, one can notice the significant improvement of the proposed algorithm with a gain between 35.9 and 48.5 % in comparison to 4D Flow MRI data and between 24 and 37.5 % to LISR. The SFSR Pearson's correlation is beneficial to the original 4D Flow MRI one with an increase between 12.6 and 35.8 % and to LISR with the improvement interval 5.5-23.8 %. PSR solution provides better performance than LISR but remains lower than SFSR in term of RMSE and correlation, especially in the lower flow rate phases. Indeed, 4D Flow MRI correlation, as long as LISR and PSR, are severely influenced by the flow variation whereas the SFSR correlation is more stable. Finally, the computation time of the factor 2 SFSR reconstruction is 15 mins by phase in average for data and SR matrices size of [94,114,28], and [187,227,55]. This time is much smaller than in the case of factor 3 (about 65 mins per phase on average).

In order to complete these performance indicators, Fig. 7 illustrates the velocity maps of the LISR, PSR and the SFSR reconstruction with a factor 2 by dimension (*i.e.* 1 mm ISO resolution), for three phases, along with their respective error maps. These figures are set with a logarithmic color scale to better represent the error localization. One can observe the expected reconstruction fidelity between SFSR, LISR and PSR solutions. Furthermore, SFSR velocities outside the fluid domain are significantly smoothed by the term $\mathcal{R}$ without degrading inside velocities. Local error remains high in the aneurysm shape region whereas the error is moderate within the arch. A detailed examination of these results led to the conclusion that the improvement is not localized on specific areas but more uniformly distributed. As a complement, Fig. 8 represents the LISR, PSR, and SFSR Bland-Altman graphs with respect to the CFD reference. It appears that the interpolated data and PSR overestimate the CFD reference for a large range of velocity magnitudes whereas SFSR underestimates more values of 20 $\mathrm{cm/s}$. Besides, SFSR outperforms LISR and PSR approaches on two aspects: the bias is reduced from 1.78 and 1.16 to -0.19 $\mathrm{cm/s}$ and the 95 % confidence interval is diminished from 19.74 and 15.84 to 15.38 $\mathrm{cm/s}$.

C. Application on a in-vivo 4D Flow MRI dataset

The proposed algorithm SFSR has been applied to a *in-vivo* dataset in order to demonstrate the SR applicability in a clinical routine context. Fig. 9 shows the LISR and SFSR results over the cardiac cycle with a focus on four regions of interest: the aortic valve (red), the ascending aorta in proximity of the pulmonary trunk (green), the aortic arch (blue), and the heart right ventricle (yellow). Although no prior segmentation were used to compute the super-resolved velocity field, one can observe a clear separation between the fluid domain and its surroundings. Besides, SFSR and LISR are efficient to distinguish two close disjoints fluid domains like the aorta and the pulmonary trunk as depicted in the green frame in Fig. 9. Complex fluid flow can be observed in the ascending aorta and the heart left ventricle. SFSR velocity field patterns in the ascending aorta are close to LISR ones whereas the velocity patterns in the right ventricle are more complex after super-resolution. Fig. 10 represents the velocity norm along the cardiac phases of four points in different regions of the aorta (cf. Fig. 9 on the top-left). Velocity peaks are important biomarkers in cardiovascular imaging and Fig. 10 demonstrates that the maximum values are preserved and even restored in the case of the point 1.

Finally, the computation time is 9 min by timeframe on average which makes SR applicability feasible in clinical routine. For note, the anatomic signal is a key information for the segmentation-free strategy, and thus the image contrast is determinant for SFSR reconstruction. PSR and SbSR solutions have not been used on this dataset since the segmentation is not available for the full cardiovascular system.

V. Discussion

This paper introduces a new super-resolution solution which reaches high quantification performance on synthetic and phantom 4D Flow MRI datasets. In addition, the segmentation-free design of that solution along with its reduced computation time are strong arguments towards clinical application.

The proposed algorithm is computationally efficient due to several aspects. First, the construction of large sparse matrices has been avoided by the use of adequate operators minimizing the memory cost. Then, these operators were applied to large 3D arrays through a GPU which reduces significantly the computation time. For the sake of balance, the reproduction of SbSR benefit also from this architectural design. Akin to the previous contribution PSR [29], SFSR smaller computation time is mainly due to the penalization formulation and the use of the *a priori* standard deviation. Indeed, the mass conservation equation constraint in SbSR involves the solving of a Poisson problem which is complex and time-consuming. SFSR formulation implies to use an implicit velocity-pressure coupling and not a segregated framework as in SbSR. The velocity-pressure coupling advantage over segregated scheme for CFD simulation has been detailed in [32]. Besides, the cardiac phase independent design of SFSR is also an asset since each phase can be computed in parallel. Although that phase independent architecture implies fluid mechanic laws approximation with the transient term omission, its impact on pulsatile flow were moderate.

On the other hand, the proposed solution SFSR achieves two major objectives which are the resolution enhancement and noise reduction even in the context of a pulsatile flow. In term of quantification, SFSR algorithm demonstrated high performance with an error reduction of a least 44.1 % in term of RMSE while improving the resolution of a factor 2 by dimension. The Pearson's correlation were superior to 82 % for both synthetic and phantom datasets. Furthermore, SFSR quantification performance are still interesting for a SR factor of 3 although the computation cost increase slightly. Finally, SFSR solution outperforms the SbSR strategy for all the performance indicators despite the use of a pre-established segmentation to define the vessel wall. In addition to these performance improvement, we demonstrate the possibility to estimate a super-resolved velocity map without any prior fluid

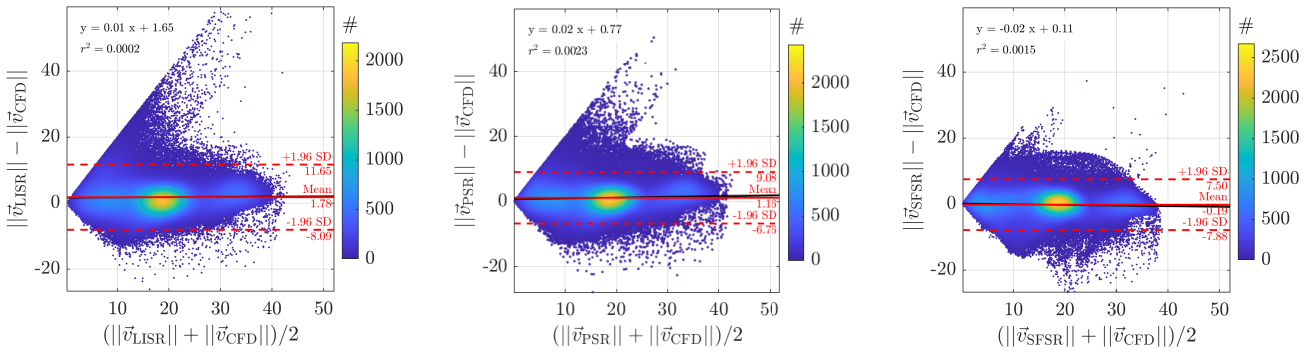

(a) Interpolated 4D Flow MRI (b) PSR (c) SFSR

Fig. 8. LISR, PSR, and SFSR solution Bland-Altman graphs with respect to the CFD reference at the systolic time $t = 322.4$ ms.

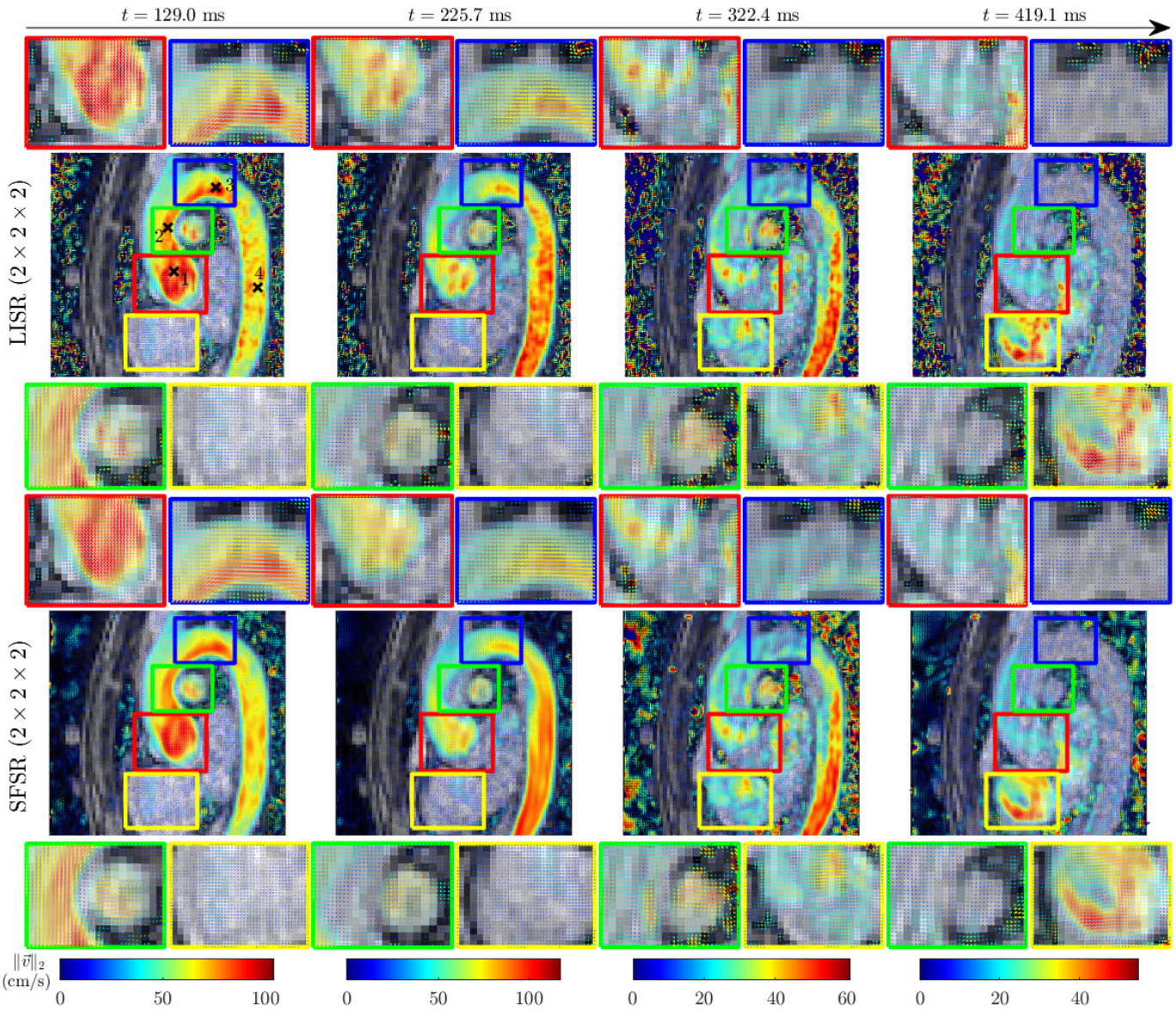

Fig. 9. LISR and SFSR super-resolved velocity during the cardiac cycle with a focus on four regions of interest, shown in red, blue, green and yellow frames.

domain knowledge where the anatomic signal acts as a soft-segmentation. Consequently, the anatomic images contrast has to be good enough to distinguish fluid area from non-fluid region. Then, 4D Flow MRI acquisitions obtained with the

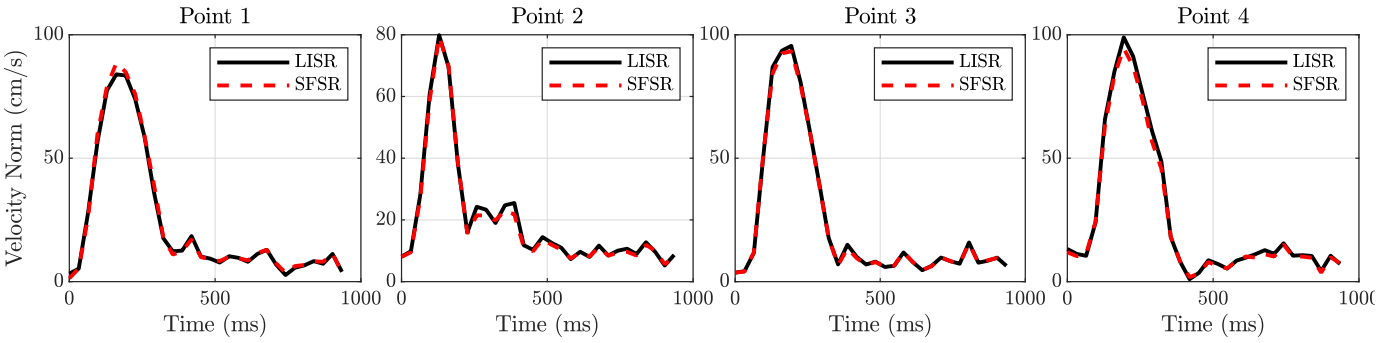

Fig. 10. LISR and SFSR velocity norm with a super-resolution of factor 2 during the cardiac cycle for the four points depicted in Figure 9.

use of contrast agent will help SFSR to perform better.

Besides, SbSR and PSR use a pre-established segmentation in order to define precisely the vessel wall and ensure the velocity nullity on the border whereas SFSR fluid domain borders are implicitly deduced. Actually, SFSR velocities at the vessel wall does not converge to zero but to a smoothed areas. Although these regions' values are generally small, the residual error close to the borders might slightly affect wall-related biomarkers such as the wall shear stress. Since RMSE is smaller for SFSR than SbSR within the whole fluid domain and also in the near-wall regions (as depicted in Fig. 5), the impact of that non-zero areas needs to be investigated directly in relation with biomarkers of interest. A recent study [40] demonstrated the correlation between wall shear stress and biomarkers of inflammation in aortic dilation, while the WSS were calculated from 4D flow MRI data with their original noise level and resolution. With SFSR, the near-wall error is reduced and then one can expect a quantification improvement of the WSS, as demonstrated in [5].

The proposed solution can be challenged by many other solution using a pre-established segmentation. Actually, segmentation methods already exist with efficient performance [27], [28]. Unfortunately, most of these segmentation methods' use a large amount of labeled data unavailable in the public domain. A segmentation-free strategy aims to reduce the labeling cost. In addition, a segmentation tool is generally designed for a specific region of interest and a segmentation-free option might allow to explore new regions or vessel malformations.

Based on the comparison between solutions using or not a prior segmentation, one can discuss the utility to determine that fluid-domain. The SFSR approach outperforms the PSR solution, even though it uses the Navier-Stokes term and exact segmentation as a priori. The study of PSR without any segmentation [29] demonstrated that a smoothing term is essential to build a segmentation-free approach. Besides, that smoothing term, which embeds fluid prior information, helps the reconstruction with more flexibility than a strict constraint. In addition, that flexibility allows to perform significantly better even when the acquisition model is over-simplified. Let notice that the acquisition model can be degraded by the use of acceleration process or because of measured artifacts such as velocity aliasing.

The proposed solution's tuning depends on penalization weights and hemodynamic parameters. Both penalization parameters α and β are essential to guarantee an efficient RMSE while controlling the fluid mechanic and smoothing terms' weights. The hemodynamic parameters modification has a negligible effect on the RMSE performance. Consequently, SFSR is mainly dependent on the two penalization weights. For a clinical use, these parameters need to be estimated over a larger amount of data with different MRI strength, reconstruction algorithm, and noise levels in order to obtain a generalization set of parameters.

Finally, SR solutions were evaluated according to the velocity accuracy whereas the relative pressure estimation is a by-product. Relative pressure is known as one the most complex biomarker to estimate [7]. In the case of SbSR, PSR, and SFSR, the relative pressure results were in most situations too noisy and inconsistent. SbSR could get the expected linear gradient of a Poiseuille flow only with a extremely low noise level. SFSR estimation might be impacted by the non-definition of the fluid domain. However, SFSR could be used as a entry for a dedicated relative pressure mapping algorithm.

Further investigations will be led on the optimization strategy with the use of descent algorithms allowing faster convergence rate and less computation time. Besides, fluid segmentation, being a tedious task, might benefit from the construction of a joint estimator providing both the super-resolved velocity field and the segmentation. In order to characterize the environment change, a different norm might be used to introduce sparsity in the smoothing term.

VI. Conclusion

This paper introduced a new segmentation-free algorithm to compute efficiently a super-resolved solution of velocity vectors from 4D Flow MRI data. The proposed SFSR solution, based on inverse problem theory, relies on two additional prior: one term using the Navier-Stokes equations ensuring realistic fluid flow reconstruction and one term smoothing the velocity outside the potential fluid domain enabling a reliable segmentation-free approach. Using penalization in contrast to hard constraint on the Navier-Stokes equations provides a computationally efficient solution which is also demonstrated by satisfying RMSE performance.

Acknowledgment

We would like to thank Thomas Puiseux, Ramiro Moreno (Spin Up - www.spin-up.fr), Franck Nicoud and Simon

Mendez (University of Montpellier) for generously letting us rely on their phantom data and thorough comparison with its specific computational fluid dynamics simulation run with the YALES2BIO solver (https://imag.umontpellier.fr/ yales2bio/).

APPENDIX A
POINT SPREAD FUNCTION COMPUTATION OVER A STAGGERED GRID

The operator $\mathbf{H}$ applies a convolution over the velocity field as depicted by the Fig. 1. Since FVM requires the use of a staggered grid to describe the velocity, each vector in $\boldsymbol{u}$, $\boldsymbol{v}$, and $\boldsymbol{w}$ is positioned at the borders between two voxels. In Fig. 1, these staggered vectors are represented in red for the u-component of the velocity and green for the v-component. In order to express each velocity components at the center of the voxel, a 1D linear interpolation has been applied in each specific direction. The resulting velocity is represented in cyan in Fig. 1. Once the super-resolved velocity components are defined on a common grid, the averaging Point Spread Function, with a kernel size equal to $2\mathrm{s}+1$, is applied on the whole image. Finally, a decimation operator is applied in order to maintain the PSF convolution centered on the data positions. To conclude, the operator $\mathbf{H}$ is the succession of three linear operations: interpolation, convolution, decimation.

APPENDIX B
NAVIER-STOKES LINEARIZATION BY FVM

In FVM, a partial differential equation is integrated over a given volume. In this work, the considered volume is a voxel defined at the super-resolved resolution. Contrary to irregular mesh, the super-resolved grid is regular and implies the use of a staggered grid description of the velocity. It means that the volume of interest to integrate has to be shifted in the velocity component direction. Both Figures 11.(a) and 11. (b) illustrate the shift applied with respect to the direction of interest. For sake of clarity, only a 2D example is represented in Fig. 11.

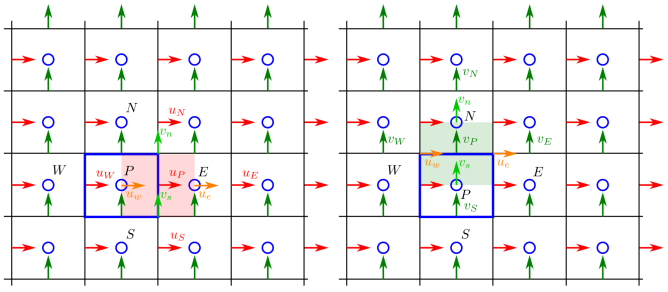

(a) Staggered grid in the u-direction (b) Staggered grid in the v-direction

Fig. 11. Illustration of the 2D staggered grid for the computation of the momentum equations.

Thanks to the FVM in a 3D context, one can express the partial differential equations of Navier-Stokes as:

$$a_P u_P = a_s u_S + a_n u_N + a_e u_E + a_w u_W + a_f u_F + a_r u_R$$
$$b_P v_P = b_s v_S + b_n v_N + b_e v_E + b_w v_W + b_f v_F + b_r v_R$$
$$c_P w_P = c_s w_S + c_n w_N + c_e w_E + c_w w_W + c_f w_F + c_r c_R$$

where the coefficients, in the Upwind integration scheme, are equal to:

$$a_e = \max(-0.5\,\rho\,\delta y\,\delta z\,u_e, 0) + \mu\delta y\,\delta z/\delta x$$
$$a_w = \max(0.5\,\rho\,\delta y\,\delta z\,u_w, 0) + \mu\,\delta y\,\delta z/\delta x$$
$$a_s = \max(-0.5\,\rho\,\delta x\,\delta z\,v_s, 0) + \mu\,\delta x\,\delta z/\delta y$$
$$a_n = \max(0.5\,\rho\,\delta x\,\delta z\,v_n, 0) + \mu\,\delta x\,\delta z/\delta y$$
$$a_r = \max(-0.5\,\rho\,\delta x\delta y\,w_r, 0) + \mu\,\delta x\,\delta y/\delta z$$
$$a_f = \max(0.5\,\rho\,\delta x\,\delta y\,w_f, 0) + \mu\,\delta x\,\delta y/\delta z$$
$$a_P = a_e + a_w + a_s + a_n + a_r + a_f$$
$$b_e = \max(-0.5\,\rho\,\delta y\,\delta z\,u_e, 0) + \mu\,\delta y\,\delta z/\delta x$$
$$b_w = \max(0.5\,\rho\,\delta y\,\delta z\,u_w, 0) + \mu\,\delta y\,\delta z/\delta x$$
$$b_s = \max(-0.5\,\rho\,\delta x\,\delta z\,v_s, 0) + \mu\,\delta x\,\delta z/\delta y$$
$$b_n = \max(0.5\,\rho\,\delta x\,\delta z\,v_n, 0) + \mu\,\delta x\,\delta z/\delta y$$
$$b_r = \max(-0.5\,\rho\,\delta x\,\delta y\,w_r, 0) + \mu\,\delta x\,\delta y/\delta z$$
$$b_f = \max(0.5\,\rho\,\delta x\,\delta y\,w_f, 0) + \mu\,\delta x\,\delta y/\delta z$$
$$b_P = b_e + b_w + b_s + b_n + b_r + b_f$$
$$c_e = \max(-0.5\,\rho\,\delta y\,\delta z\,u_e, 0) + \mu\,\delta y\,\delta z/\delta x$$
$$c_w = \max(0.5\,\rho\,\delta y\,\delta z\,u_w, 0) + \mu\,\delta y\,\delta z/\delta x$$
$$c_s = \max(-0.5\,\rho\,\delta x\,\delta z\,v_s, 0) + \mu\,\delta x\,\delta z/\delta y$$
$$c_n = \max(0.5\,\rho\,\delta x\,\delta z\,v_n, 0) + \mu\,\delta x\,\delta z/\delta y$$
$$c_r = \max(-0.5\,\rho\,\delta x\,\delta y\,w_r, 0) + \mu\,\delta x\,\delta y/\delta z$$
$$c_f = \max(0.5\,\rho\,\delta x\,\delta y\,w_f, 0) + \mu\,\delta x\,\delta y/\delta z$$
$$c_P = c_e + c_w + c_s + c_n + c_r + c_f$$

All these coefficients need to be computed for each voxel and are the non-zero elements of the sparse $\mathbf{S}_{\mathcal{X}}$ matrix. Moreover, these coefficient are different across voxels since their values depend on the velocity at each voxel position. Numerically, these coefficients have been stored in 3D arrays and used through element-wise primitive operation that are particularly suitable for GPU computing.

REFERENCES

[1] M. Markl, A. Frydrychowicz, S. Kozerke, M. Hope, and O. Wieben, "4D Flow MRI," *J. Magn. Reson. Imaging*, vol. 36, no. 5, pp. 1015–1036, 2012. [Online]. Available: http://dx.doi.org/10.1002/jmri.23556

[2] A. Wåhlin, A. Eklund, and J. Malm, "4D flow MRI hemodynamic biomarkers for cerebrovascular diseases," *J. Intern. Med.*, vol. 291, no. 2, pp. 115–127, 2022. [Online]. Available: https://onlinelibrary.wiley.com/doi/abs/10.1111/joim.13392

[3] N. J. Pelc, M. A. Bernstein, A. Shimakawa, and G. H. Glover, "Encoding strategies for three-direction phase-contrast MR imaging of flow," *J. Magn. Reson. Imaging*, vol. 1, no. 4, pp. 405–413, 1991. [Online]. Available: http://dx.doi.org/10.1002/jmri.1880010404

[4] A. F. Stalder, M. F. Russe, A. Frydrychowicz, J. Bock, J. Hennig, and M. Markl, "Quantitative 2D and 3D phase contrast MRI: Optimized analysis of blood flow and vessel wall parameters," *Mag. Reson. Med.*, vol. 60, no. 5, pp. 1218–1231, 2008. [Online]. Available: http://dx.doi.org/10.1002/mrm.21778

[5] S. Levilly, M. Castagna, J. Idier, F. Bonnefoy, D. Le Touzé, S. Moussaoui, P. Paul-Gilloteaux, and J.-M. Serfaty, "Towards quantitative evaluation of wall shear stress from 4D flow imaging," *Magn. Reson. Imaging*, vol. 74, pp. 232–243, 2020. [Online]. Available: https://www.sciencedirect.com/science/article/pii/S0730725X20300230

[6] Q. Gao, X. Liu, H. Wang, P. Wu, M. Jin, R. Wei, W. Wang, Z. Niu, S. Zhao, and F. Li, "Optimization of 4d flow mri velocity field in the aorta with divergence-free smoothing," *Medical & Biological Engineering & Computing*, vol. 59, pp. 2237–2252, 2021.

[7] S. B. Krittian, P. Lamata, C. Michler, D. A. Nordsletten, J. Bock, C. P. Bradley, A. Pitcher, P. J. Kilner, M. Markl, and N. P. Smith, "A finite-element approach to the direct computation of relative cardiovascular pressure from time-resolved MR velocity data," *Med. Image Anal.*, vol. 16, no. 5, pp. 1029–1037, 2012. [Online]. Available: https://www.sciencedirect.com/science/article/pii/S1361841512000497

[8] M. F. Fathi, A. Bakhshinejad, A. Baghaie, D. Saloner, R. H. Sacho, V. L. Rayz, and R. M. D'Souza, "Denoising and spatial resolution enhancement of 4D flow MRI using proper orthogonal decomposition and lasso regularization," *Comput. Med. Imaging Graph.*, vol. 70, pp. 165 – 172, 2018. [Online]. Available: http://www.sciencedirect.com/science/article/pii/S089561111830257X

[9] I. Perez-Raya, M. F. Fathi, A. Baghaie, R. H. Sacho, K. M. Koch, and R. M. D'Souza, "Towards multi-modal data fusion for super-resolution and denoising of 4D-flow MRI," *Int. J. Numer. Meth. Bio.*, vol. 36, no. 9, 2020. [Online]. Available: https://onlinelibrary.wiley.com/doi/abs/10.1002/cnm.3381

[10] E. Ferdian, A. Suinesiaputra, D. J. Dubowitz, D. Zhao, A. Wang, B. Cowan, and A. A. Young, "4DFlowNet: Super-resolution 4D flow MRI using deep learning and computational fluid dynamics," *AIP Conf. Proc.*, vol. 8, p. 138, 2020. [Online]. Available: https://www.frontiersin.org/article/10.3389/fphy.2020.00138

[11] L. Boussel, V. L. Rayz, A. Martin, G. Acevedo-Bolton, M. T. Lawton, R. Higashida, W. S. Smith, W. L. Young, and D. Saloner, "Phase-contrast magnetic resonance imaging measurements in intracranial aneurysms in vivo of flow patterns, velocity fields, and wall shear stress: comparison with computational fluid dynamics." *Mag. Reson. Med.*, vol. 61, pp. 409–417, 02 2009.

[12] A. Bakhshinejad, V. L. Rayz, and R. M. D'Souza, "Reconstructing blood velocity profiles from noisy 4D-PCMR data using ensemble kalman filtering," in *Biomedical Engineering Society (BMES) 2016 Annual Meeting, Minneapolis, MN, USA*, 10 2016.

[13] A. Bakhshinejad, A. Baghaie, A. Vali, D. Saloner, V. L. Rayz, and R. M. D'Souza, "Merging computational fluid dynamics and 4D flow MRI using proper orthogonal decomposition and ridge regression," *J. Biomech.*, vol. 58, pp. 162–173, 2017.

[14] F. Gaidzik, D. Stucht, C. Roloff, O. Speck, D. Thévenin, and G. Janiga, "Transient flow prediction in an idealized aneurysm geometry using data assimilation," *Comput. Biol. Med.*, vol. 115, 2019. [Online]. Available: http://www.sciencedirect.com/science/article/pii/S0010482519303713

[15] S. Saitta, M. Carioni, S. Mukherjee, C.-B. Schönlieb, and A. Redaelli, "Implicit neural representations for unsupervised super-resolution and denoising of 4D flow MRI," *Comput. Meth. Prog. Bio.*, p. 108057, 2024.

[16] S. Shit, J. Zimmermann, I. Ezhov, J. C. Paetzold, A. F. Sanches, C. Pirkl, and B. H. Menze, "Srflow: Deep learning based super-resolution of 4d-flow mri data," *Frontiers in Artificial Intelligence*, vol. 5, 2022. [Online]. Available: https://www.frontiersin.org/articles/10.3389/frai.2022.928181

[17] N. de Hoon, R. van Pelt, A. Jalba, and A. Vilanova, "4D MRI flow coupled to physics-based fluid simulation for blood-flow visualization," *Comput. Graph. Forum*, vol. 33, no. 3, pp. 121–130, 2014. [Online]. Available: https://onlinelibrary.wiley.com/doi/abs/10.1111/cgf.12368

[18] F. M. Callaghan and S. M. Grieve, "Spatial resolution and velocity field improvement of 4D-flow MRI," *Mag. Reson. Med.*, vol. 78, no. 5, pp. 1959–1968, 2017. [Online]. Available: https://onlinelibrary.wiley.com/doi/abs/10.1002/mrm.26557

[19] V. C. Rispoli, J. F. Nielsen, K. S. Nayak, and J. L. Carvalho, "Computational fluid dynamics simulations of blood flow regularized by 3D phase contrast MRI," *Biomed. Eng. Online*, vol. 14, no. 1, p. 110, 2015.

[20] M. D'Elia, M. Perego, and A. Veneziani, "A variational data assimilation procedure for the incompressible Navier-Stokes equations in hemodynamics," *J. Sci. Comput.*, vol. 52, no. 2, pp. 340–359, 2012. [Online]. Available: http://dx.doi.org/10.1007/s10915-011-9547-6

[21] S. W. Funke, M. Nordaas, O. Evju, M. S. Alnæs, and K. A. Mardal, "Variational data assimilation for transient blood flow simulations: Cerebral aneurysms as an illustrative example," *Int. J. Numer. Meth. Bio.*, vol. 35, no. 1, 2019. [Online]. Available: https://onlinelibrary.wiley.com/doi/abs/10.1002/cnm.3152

[22] N. de Hoon, A. Jalba, E. Farag, P. van Ooij, A. Nederveen, E. Eisemann, and A. Vilanova, "Data assimilation for full 4D PC-MRI measurements: Physics-based denoising and interpolation," *Comput. Graph. Forum*, vol. 39, no. 6, pp. 496–512, 2020. [Online]. Available: https://onlinelibrary.wiley.com/doi/abs/10.1111/cgf.14088

[23] J. Töger, M. J. Zahr, N. Aristokleous, K. Markenroth Bloch, M. Carlsson, and P.-O. Persson, "Blood flow imaging by optimal matching of computational fluid dynamics to 4D-flow data," *Magn. Reson. Med.*, vol. 84, no. 4, pp. 2231–2245, 2020. [Online]. Available: https://onlinelibrary.wiley.com/doi/abs/10.1002/mrm.28269

[24] M. F. Fathi, I. Perez-Raya, A. Baghaie, P. Berg, G. Janiga, A. Arzani, and R. M. D'Souza, "Super-resolution and denoising of 4D-flow MRI using physics-informed deep neural nets," *Comput. Meth. Prog. Bio.*, p. 105729, 2020. [Online]. Available: http://www.sciencedirect.com/science/article/pii/S0169260720315625

[25] T. Ichimura, S. Yamada, Y. Watanabe, H. Kawano, and S. Ii, "A practical approach for estimation of patient-specific intra-aneurysmal flows using variational data assimilation," *medRxiv*, 2024. [Online]. Available: https://www.medrxiv.org/content/early/2024/05/26/2024.05.24.24307838

[26] J. Idier, *Bayesian Approach to Inverse Problems*. ISTE Ltd and John Wiley & Sons Inc, Apr. 2008.

[27] H. Berhane, M. Scott, M. Elbaz, K. Jarvis, P. McCarthy, J. Carr, C. Malaisrie, R. Avery, A. J. Barker, J. D. Robinson, C. K. Rigsby, and M. Markl, "Fully automated 3D aortic segmentation of 4D flow MRI for hemodynamic analysis using deep learning," *Magn. Reson. Medicine*, vol. 84, no. 4, pp. 2204–2218, 2020. [Online]. Available: https://onlinelibrary.wiley.com/doi/abs/10.1002/mrm.28257

[28] M. Bustamante, F. Viola, J. Engvall, C.-J. Carlhäll, and T. Ebbers, "Automatic time-resolved cardiovascular segmentation of 4D flow MRI using deep learning," *J. of Magn. Reson. Imaging*, vol. 57, no. 1, pp. 191–203, 2023. [Online]. Available: https://onlinelibrary.wiley.com/doi/abs/10.1002/jmri.28221

[29] S. Levilly, S. Moussaoui, and J.-M. Serfaty, "Navier-stokes-based regularization for 4D flow MRI super-resolution," in *Proc. IEEE 19th I. S. Biomed. Imaging (ISBI)*, 2022.

[30] T. Puiseux, A. Sewonu, O. Meyrignac, H. Rousseau, F. Nicoud, S. Mendez, and R. Moreno, "Reconciling PC-MRI and CFD: An in-vitro study," *NMR Biomed*, vol. 32, no. 5, p. e4063, 2019. [Online]. Available: https://analyticalsciencejournals.onlinelibrary.wiley.com/doi/abs/10.1002/nbm.4063

[31] S. V. Patankar, *Numerical Heat Transfer and Fluid Flow*. Hemisphere Publishing Corporation, 1980.

[32] Z. Mazhar, *Fully Implicit, Coupled Procedures in Computational Fluid Dynamics*. Springer, Cham, 2016, vol. 115.

[33] J. Bock, A. Frydrychowicz, A. F. Stalder, T. A. Bley, H. Burkhardt, J. Hennig, and M. Markl, "4D phase contrast MRI at 3T: Effect of standard and blood-pool contrast agents on SNR, PC-MRA, and blood flow visualization," *Magn. Reson. Med.*, vol. 63, no. 2, pp. 330–338, 2010. [Online]. Available: https://onlinelibrary.wiley.com/doi/abs/10.1002/mrm.22199

[34] S. Levilly, S. Moussaoui, and J.-M. Serfaty, "Segmentation-free super-resolved 4D flow MRI reconstruction exploiting Navier-Stokes equations and spatial regularization," in *Proc. 29th IEEE Image Proc. (ICIP)*, 2022, pp. 2316–2320.

[35] A. T. Hess, M. M. Bissell, N. A. Ntusi, A. J. Lewis, E. M. Tunnicliffe, A. Greiser, A. F. Stalder, J. M. Francis, S. G. Myerson, S. Neubauer, and M. D. Robson, "Aortic 4D flow: Quantification of signal-to-noise ratio as a function of field strength and contrast enhancement for 1.5T, 3T, and 7T," *Magn Reson Med*, vol. 73, no. 5, pp. 1864–1871, 2015. [Online]. Available: https://onlinelibrary.wiley.com/doi/abs/10.1002/mrm.25317

[36] S. Mendez, A. Bérod, C. Chnafa, M. Garreau, E. Gibaud, A. Larroque, S. Lindsey, M. Martins Afonso, P. Mattéoli, R. Mendez Rojano, D. Midou, T. Puiseux, J. Sigüenza, P. Taraconat, V. Zmijanovic, and F. Nicoud, *YALES2BIO: A General Purpose Solver Dedicated to Blood Flows*. John Wiley & Sons, Ltd, 2022, ch. 7, pp. 183–206. [Online]. Available: https://onlinelibrary.wiley.com/doi/abs/10.1002/9781119986607.ch7

[37] M. A. Bernstein, X. J. Zhou, J. A. Polzin, K. F. King, A. Ganin, N. J. Pelc, and G. H. Glover, "Concomitant gradient terms in phase contrast MR: Analysis and correction," *Magn. Reson. Med.*, vol. 39, no. 2, pp. 300–308, 1998. [Online]. Available: https://onlinelibrary.wiley.com/doi/abs/10.1002/mrm.1910390218

[38] P. Connes, T. Alexy, J. Detterich, M. Romana, M.-D. Hardy-Dessources, and S. K. Ballas, "The role of blood rheology in sickle cell disease," *Blood Rev.*, vol. 30, no. 2, pp. 111–118, 2016. [Online]. Available: https://www.sciencedirect.com/science/article/pii/S0268960X15000661

[39] T. Kenner, "The measurement of blood density and its meaning," *Basic Res. Cardiol.*, vol. 84, pp. 111–124, 1989.

[40] F. Hammaréus, C. Trenti, H. M. Björck, J. Engvall, H. Lekedal, A. Krzynska-Trzebiatowska, D. Kylhammare, M. Lindenberger, A. K. Lundberg, F. Nilsson, L. Nilsson, E. Swahn, L. Jonasson, and P. Dyverfeldt, "Wall Shear Stress Measured with 4D Flow CMR Correlates with Biomarkers of Inflammation and Collagen Synthesis in Mild-to-Moderate Ascending Aortic Dilation and Tricuspid Aortic Valves," *European Heart Journal - Cardiovascular Imaging*, p. 130, 05 2024. [Online]. Available: https://doi.org/10.1093/ehjci/jeae130